Aharonov-Bohm effect in monolayer phosphorene nanorings

Rui Zhang,[1,2] Zhenhua Wu,[3,*] X. J. Li,[4] and Kai Chang[1,2,†]

[1]*SKLSM, Institute of Semiconductors, Chinese Academy of Sciences, 100083 Beijing, China*

[2]*College of Materials Science and Opto-Electronic Technology, University of Chinese Academy of Sciences, 100049 Beijing, China*

[3]*Key Laboratory of Microelectronic Devices and Integrated Technology, Institute of Microelectronics, Chinese Academy of Sciences, 100029 Beijing, China*

[4]*College of Physics and Energy, Fujian Normal University, 350007 Fuzhou, China*

(Received 28 October 2016; revised manuscript received 12 January 2017; published 13 March 2017)

This work presents a theoretical demonstration of the Aharonov-Bohm (AB) effect in monolayer phosphorene nanorings (PNRs). Atomistic quantum transport simulations of PNRs are employed to investigate the impact of multiple modulation sources on the sample conductance. In the presence of a perpendicular magnetic field, we find that the conductance of both armchair and zigzag PNRs oscillate periodically in a low-energy window as a manifestation of the AB effect. Our numerical results reveal a giant magnetoresistance (MR) in zigzag PNRs (with a maximum magnitude approaching 2000%). It is attributed to the AB-effect-induced destructive interference phase over a wide energy range below the bottom of the second subband. We also demonstrate that PNR conductance is highly anisotropic, offering an additional way to modulate MR. The giant MR in PNRs is maintained at room temperature in the presence of the thermal broadening effect.

DOI: 10.1103/PhysRevB.95.125418

I. INTRODUCTION

Phosphorene, the single- and few-layer form of black phosphorus (BP), has been successfully fabricated by researchers very recently [1–3]. It holds great promise for applications in electronics and optoelectronics because of its excellent mechanical, optical, thermoelectric, and electronic properties [1–15]. BP is the most stable allotrope among the phosphorus group, which also includes white, red, and violet phosphorus [16,17]. It consists of phosphorus atom layers coupled by weak van der Waals interlayer interactions. Bulk BP possesses a direct band gap; this direct gap increases when the film thickness decreases from bulk to a few layers and, eventually, to a monolayer via mechanical exfoliation. Due to its unique structure in two-dimensional (2D) materials family, the band structure, electrical conductivity, thermal conductivity, and optical responses of phosphorene are highly anisotropic [2,7,15,18,19], which is different from other widely studied 2D materials such as graphene, monolayer boron nitride, silicene, and transition metal dichalcongenide.

As a newly emerged member of the 2D crystal family, phosphorene ignited a surge of research activities in the physics, chemistry, and materials communities because of its interesting unique physical properties and its potential application in the future. Various properties of phosphorene have been investigated theoretically and experimentally, e.g., the field transistor effect [1,3,4,20], strain modification [7,13,19,21], optoelectronics and electronics [22–31], transport properties [2,32,33], excitons [18,34], and heterostructures and PN junctions [35–37], and a recent experiment demonstrated crystalline anisotropy impacted phase-coherent transport properties in BP field-effect transistors [38]. Another experiment, carried out by Masih Das *et al.* [39] indicates that it is possible to sculpture phosphorus nanoribbons experimentally, which provides the possibility of making a phosphorene nanoring (PNR) as proposed in this paper.

The Aharonov-Bohm (AB) effect [40] is an important phenomenon in quantum physics which has garnered great attentions in past decades. The AB effect in graphene nanostructures including graphene nanoribbons [41], nanotube [42], and graphene nanorings [43–46] has been investigated.

However, the AB effect in PNRs remains unexplored, so in this work we theoretically investigate the transport properties of monolayer PNRs utilizing the tight-binding (TB) method and recursive Green's function method. Transport properties of nanorings with different crystalline orientations, temperatures, incident energies, and magnetic felds are calculated. We find that the crystalline orientation of a nanoring greatly affects the quantum tunneling behavior and the value of magnetoresistance (MR), i.e., the MR is highly anisotropic in PNRs. Resonant tunneling can be obtained in both armchair and zigzag PNRs.

The paper is organized as follows. In Sec. II, we present the TB model and the algorithm with which we calculate the transport properties of the system. In Sec. III, we briefly discuss the physics of the AB effect and investigate the AB effect in PNRs. The MR of PNRs is demonstrated in Sec. IV. Finally, we summarize our results in Sec. V.

II. MODEL AND FORMULATION

In monolayer phosphorene each phosphorus atom is covalently bonded with three adjacent phosphorus atoms to form a low-puckered honeycomb structure. Phosphorene has an irregular honeycomb structure with lattice constants $a = 4.38$ Å and $b = 3.31$ Å. There are four phosphorus atoms in a unit cell. The TB Hamiltonian for the PNRs can be written as [23]

$$H_C = \sum_{i \neq j} t_{i,j} c_i^\dagger c_j, \tag{1}$$

where the summation runs over all the lattice sites of PNRs, $c_i^\dagger$ (c_j) is the creation (annihilation) operator of the electron at site i (j), and $t_{i,j}$ are the hopping energies. Five hopping links must be taken into consideration [23]. The related hopping

*wuzhenhua@ime.ac.cn

†kchang@semi.ac.cn

integrals are $t_1 = -1.220$ eV, $t_2 = 3.655$ eV, $t_3 = -0.205$ eV, $t_4 = -0.105$ eV, and $t_5 = -0.055$ eV. The band gap of the monolayer phosphorene given by this TB model is 1.52 eV, with the valence-band maximum and conduction-band minimum located at -1.18 and 0.34 eV, respectively [31]. When we consider a magnetic field B applied perpendicularly to the plane of a PNR, the transfer integral becomes $\widetilde{t}_{i,j} = t_{i,j}e^{i\phi_{i,j}}$, where $\phi_{i,j} = \frac{e}{\hbar}\int_{r_i}^{r_j} d\mathbf{l}\cdot\mathbf{A}$ is the Peierls phase. As we use the Peierls substitution, which means that the magnetic field is applied not only to the hole in the nanoring but also to the lattice in the nanoring; this means that the electrons in the nanoring feel a field as $\vec{B}\neq 0$, $\vec{A}\neq 0$, the nonlocal part of the AB effect mentioned in Ref. [40], is still reserved because of the magnetic flux across the big hole in the nanoring, which can be felt by the electron in the nanoring too. In our calculation, the magnetic field $\vec{B}$ is homogeneous, we take the Landau gauge, and the vector potential $\vec{A} = (0, Bx, 0)$. The magnetic flux $\phi = \frac{Bab}{2}$ through a plaquette is in units of $\phi_0 = \frac{\hbar}{e}$.

The system is composed of a central mesoscopic conductor, i.e., the PNR and two semi-infinite leads. For a large PNR, the dimension of the Hamiltonian matrix H_C is huge, and the recursive Green's function algorithm is adapted in this work. We start by dividing the system into vertical principal slices. The interaction only exists in/between adjacent slices. The Hamiltonian matrix block of the first slice, containing the self-energy of the left lead, is inverted and added to the block of the next slice to its right. This procedure is repeated until we add the block of the last slice, which contains the self-energy of the right lead. The conductance is associated with the scattering properties of the electron through the conductor region and is determined by the transmission probability via the Landauer Büttiker formula [47,48]

$$G = \frac{2e^2}{h}T, \tag{2}$$

where the conductance G and transmission probability T both depend on the incident energy E_f. In the following we adopt $G_0 = \frac{2e^2}{h}$ as the unit of conductance. The transmission probability T can be expressed in terms of the Green functions of the conductor and the coupling of the conductor to the leads,

$$T = Tr\left(\Gamma_L G_C^r \Gamma_R G_C^a\right), \tag{3}$$

where the advanced Green function G_C^a is the Hermitian conjugate of the retarded Green function G_C^r of the conductor, and $\Gamma_{L,R}$ describe the coupling between the conductor and the leads. To compute the Green function of the conductor, we can write the expression for the retarded Green function of a system:

$$G_C^r = [(E + i\eta) - H_C - \Sigma_L - \Sigma_R]^{-1}, \tag{4}$$

where E is the quasiparticle energy measured with respect to the Fermi level E_f, and η is a positive infinitesimal number defining the "retarded" character of the Green function. H_C is the Hamiltonian matrix of the finite isolated conductor, and $\Sigma_{L,R}$ are the retarded self-energy terms due to the conductor coupling with the semi-infinite leads. The self-energy terms are defined as

$$\Sigma_L = H_{LC}^{+} g_L H_{LC}, \Sigma_R = H_{RC}^{+} g_R H_{RC}, \tag{5}$$

where H_{LC} and H_{CR} represent the coupling matrices with nonzero elements only for adjacent lattices in the conductor and leads accounting for the nearest-neighbor TB approximation. g_L and g_R are the surface Green functions of the left and right semi-infinite leads. The self-energy term can be regarded as an effective Hamiltonian that arises from the coupling of the conductor with leads. The key to the problem is how to obtain the surface Green functions of the semi-infinite leads. Once the surface Green functions of the leads are known, the matrices $\Gamma_{L,R}$ can be easily obtained as

$$\Gamma_{L,R} = i\left[\Sigma_{L,R}^r - \Sigma_{L,R}^a\right], \tag{6}$$

with the advanced self-energy $\Sigma_{L,R}^r$.

From Green's function, the local density of states (LDOS) at site i can be found,

$$\rho_i = -\frac{1}{\Pi} Im[G_{i,i}], \tag{7}$$

where $G_{i,i}$ is the matrix element of Green's function at site i.

To obtain the electron transport properties at finite temperature (T), we use the nonzero temperature linear response formula,

$$G(E_F) = \frac{e^2}{\pi\hbar}\int T(E) F_T(E - E_F) dE, \tag{8}$$

where $F_T(E - E_F) = -df(E)/dE$ is the thermal broadening function and $f(E)$ is the Fermi-Dirac distribution function.

The magnetoresistance is defined as

$$R_M(E_F, B) \equiv [G(E_F, 0) - G(E_F, B)]/G(E_F, B). \tag{9}$$

Here $G(E_F, B)$ is the conductance of the system in a perpendicular magnetic field B with incident energy E_F.

III. AHARONOV-BOHM EFFECT

When we investigate the AB effect in a nanoring, there is gauge freedom in the choice of vector potential for a given magnetic field. The Hamiltonian is gauge invariant, which means that adding the gradient of a scalar field to $\vec{A}$ changes the overall phase of the wave function by an amount corresponding to the scalar field; physical properties are not influenced by the specific choice of gauge. As we choose the Landau gauge in our calculations, we have $\vec{B} = \nabla \times \vec{A}$, which is simply the definition of the vector potential, and

$$\oint_C \vec{A}\cdot d\vec{r} = \int_S (\nabla \times \vec{A})\cdot d\vec{S} = \int_S \vec{B}\cdot d\vec{S} = \phi_m, \tag{10}$$

which is a consequence of the Stokes theorem. ϕ_m is the total magnetic flux through encircled by path I and path II shown in Fig. 1. When electrons are transmitted through paths I and II (Fig. 1) in the presence of a magnetic field and finally combine in the right lead, the magnetic interference phase is $e^{i\Delta\phi}$,

$$\begin{aligned}\Delta\phi &= \frac{e}{\hbar}\left[\int_{C_I} \vec{A}(\vec{r})\cdot d\vec{r} - \int_{C_{II}} \vec{A}(\vec{r})\cdot d\vec{r}\right] \\ &= \frac{e}{\hbar}\oint_C \vec{A}(\vec{r})\cdot d\vec{r} \\ &= \frac{e}{\hbar}\int_S \vec{B}\cdot d\vec{S}.\end{aligned}$$

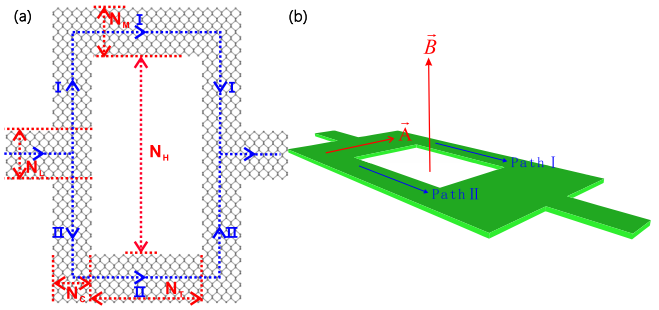

FIG. 1. Schematic of a rectangular PNR subjected to a magnetic flux threading the PNR. (a) The parameters are in units of the lattice constants **a** and **b**. In this example, a zigzag-edged nanoring, $N_L = 4$, $N_M = 4$, $N_C = 4$, $N_T = 12$, $N_H = 16$. The parameters are in units of the lattice constants **a** and **b**. (b) A uniform magnetic field is applied perpendicular to the PNR. We use the Landau gauge $\vec{A} = (0, Bx, 0)$. Electrons are transported through the central PNR via both path I and path II and then recombine in the right lead.

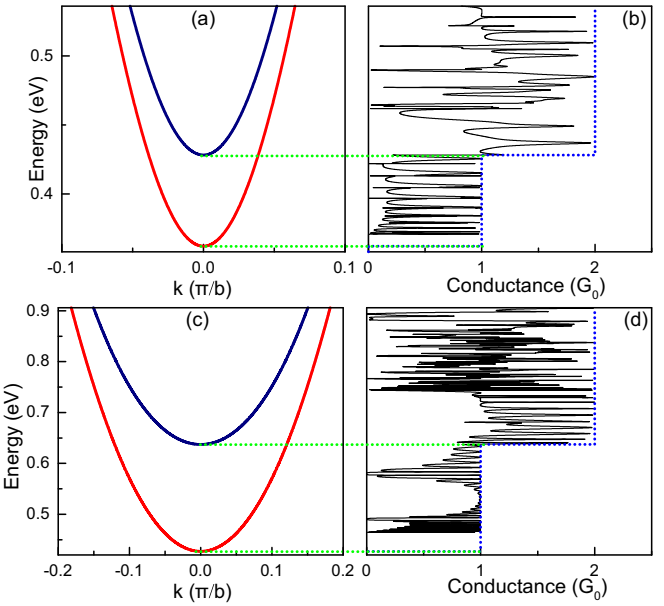

FIG. 2. Band structure of the lead and transport properties (a, b) for armchair PNRs and (c, d) for zigzag PNRs.

Here we do not discuss the normal interference phase when electrons are transmitted through paths I and II in the absence of a magnetic field.

The interference phase $\Delta\phi = \frac{e}{\hbar} B(S_h + S_l)$, $S_h + S_l$ is the total area encircled by paths I and II, S_h is the area of the hole in the nanoring, and S_l is the remaining part encircled by the path on the phosphorene lattice. S_l is determined by the incident energy, as for different incident energies the paths are different. $\frac{e}{\hbar} B S_h$ is the nonlocal part of the Aharonov-Bohm effect.

The size of the rectangular PNRs are characterized by the parameters shown in Fig. 1; the parameters are in units of phosphorene lattice constant **a** or **b**. Normally, people can simulate relatively small systems with the recursive Green's function method, due to the cubic scaling of the computational burden associated with matrix inversion. In this work, we use the recursive Green's function method, which cuts the whole system into many slices and in which the matrix inversion is calculated for each slice instead of the whole system. So this method enables the simulation of very long systems and is preferred to the study of quasi-one-dimensional systems, such as nanotubes and nanoribbons. Therefore, in this paper we consider PNRs which are narrow but relatively long. Two sets of structure parameters are taken; the first set is $N_L = 13$, $N_M = 11$, $N_C = 11$, $N_T = 120$, $N_H = 7$, and the second set is $N_L = 13$, $N_M = 22$, $N_C = 22$, $N_T = 240$, $N_H = 14$. The average area of the nanoring is given by $\bar{S} = (S_{\text{inn}} + S_{\text{out}})/2$, which is the average area of the inner (S_{inn}) and outer (S_{out}) rings. Then the average area of the first kind of PNR is $\bar{S} \approx 359.4\ \text{nm}^2$; the average area of another kind of PNR is four times that of the first kind. In the remainder, the calculations are based on the first kind of PNR without specification, as only one simulation result is based on the second kind of PNR.

First, we calculate the band structure of the lead (semi-infinite nanoribbons) and the conductance of the nanorings in the absence of magnetic fields at zero temperature. Figures 2(a) and 2(c) show the band dispersion of the lowest two conduction subbands of perfect armchair and zigzag ribbons, respectively. Unlike graphene nanoribbons, both armchair and zigzag PNRs possess finite band gaps. Accordingly the conductance of armchair/zigzag PNRs is fully suppressed when the electron incident energy E_F is below the bottom of the first subband, i.e., 0.37/0.47 eV, as shown in Figs. 2(b) and 2(d). These low-energy transmission-forbidden regions arise from the absence of propagating modes in the leads, as we use a semi-infinite phosphorene nanoribbon as the lead, so when the incident energy is below the conduction-band minimum of the lead or the lowest unoccupied molecular orbital of the nanoring, transmission is forbidden.

As the incident Fermi energy increases, we observe intensive oscillations caused by the Fabry-Perot resonant modes formed in the PNRs. Many valleys with zero or near-zero conductance are observed, arising from the absence of bound states in the central PNRs instead of the lack of propagating modes in the leads. The conductance also exhibits steplike behavior in agreement with the opening of new subbands. Let us take the armchair PNR, for example, as shown in Fig. 2(b). When $0.37\ \text{eV} < E_F < 0.43\ \text{eV}$, the conductance of the ring can reach G_0, i.e., resonant conductance peaks. For higher incident energies, in the range of $0.43\ \text{eV} < E_F < 0.6\ \text{eV}$, the conductance oscillations become more complex and disordered, and the peaks approach $2G_0$ as the second subbands start to contribute to the total conductance. Note that the main purpose of this work is to investigate the phase-coherent transport of the carriers in PNRs. It is preferable to examine an energy region in which only one mode is engaged in electron transport. Hence, we present only the results with an energy area corresponding to the first conduction subbands for both armchair and zigzag PNRs when we discuss AB oscillations and MR in PNRs.

The AB oscillations in mesoscopic rings are of particular interest and offer an elegant way to study phase-coherent electron transport properties. In the presence of a perpendicular magnetic field **B**, electrons pass through either side of the PNR (paths I and II shown in Fig. 1) and this difference produces the phase modulation: $\Delta\phi = \frac{e}{\hbar} BS$. Therefore, the

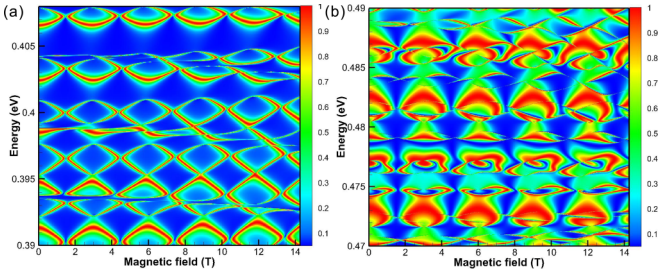

FIG. 3. Conductance of (a) armchair and (b) zigzag PNRs with structure parameters $N_L = 13$, $N_M = 22$, $N_C = 22$, $N_T = 240$, and $N_H = 14$ at temperature $T = 0$.

transmission probability through the PNR exhibits periodic oscillations when the magnetic field is varied, with a fixed period of $\Delta \boldsymbol{B} = 2\pi\phi_0/S$.

Next, we address that the conductance of a PNR not only exhibits resonant behavior with incident Fermi energy due to the formation of Fabry-Perot modes but also oscillates with a perpendicular magnetic field arising from the formation of Landau levels and AB interference. Figures 3(a) and 3(b) show contour plots of the conductance as a function of the incident Fermi energy and the magnetic field in armchair and zigzag PNRs, respectively, with structure parameters $N_L = 13$, $N_M = 22$, $N_C = 22$, $N_T = 240$, $N_H = 14$. The effect area of these two nanorings are relatively large, therefore the AB oscillation period $\Delta \boldsymbol{B}$ will be relatively small, which can be realized experimentally. From the contour plot we can see that the conductance of the PNRs oscillates both with the incident energy and with the magnetic field. The conductance oscillates with the incident energy because of resonant tunneling and oscillates with the magnetic field because of the AB effect. We find that the AB oscillation periods at different incident energies are slightly different. The reason for this difference is that for different incident energies the charge distributions in the arms of the central PNR are different and thus the effective areas encircled by path I and path II (Fig. 1) are different. In Fig. 3, the incident energy is in the interval where only the first conduction subband of the bulk states takes place. In this case, the PNR area can be approximated by $\bar{S}$ defined before, which is about 1437.6 nm^2, then the oscillation period should be $\Delta B \approx 2.88$ T. The numerical results for ΔB shown in both Fig. 3(a) and Fig. 3(b) are about 3 T, which matches the theoretical prediction well. In the following part, we illustrate this effect in more detail.

In Fig. 4(a), we plot the conductance of an armchair PNR as a function of the magnetic field strength **B** and the Fermi energy E_F with structure parameters $N_L = 13$, $N_M = 11$, $N_C = 11$, $N_T = 120$, $N_H = 7$ at zero temperature $T = 0$. The conductance of the armchair PNR oscillates periodically in magnetic field B. The period of 12 T is consistent with the expectation ($\Delta \boldsymbol{B} = 2\pi\phi_0/\bar{S}$), accounting for the area of our PNR as a manifestation of the AB effect. Importantly, the conductance peaks or valleys appear synchronously in magnetic fields with varied E_F, since the phase modulation depends on the magnetic flux through the PNR area rather than the incident energy. In such a small energy interval the effective PNR areas encircled by path I and path II all approximate to $\bar{S}$. Due to the contribution from both

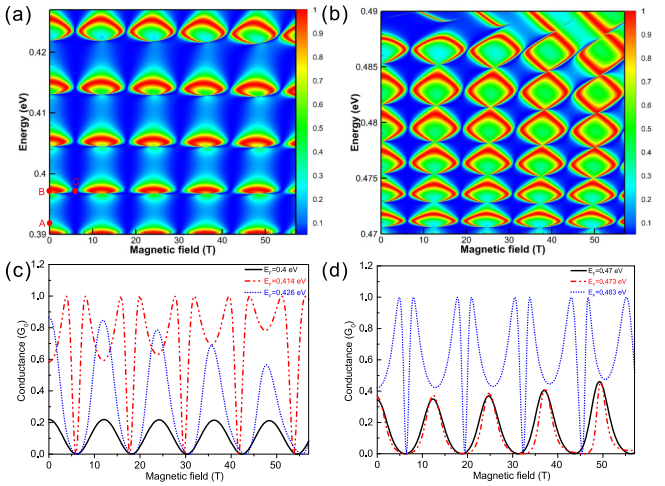

FIG. 4. Contour plot of the conductance as a function of the magnetic field and Fermi energy at temperature $T = 0$ for (a) armchair and (b) zigzag nanorings. The conductance with different incident energies at $T = 0$ for (c) armchair and (d) zigzag nanorings.

Fabry-Perot resonant and AB oscillations, the contour plot of the conductance exhibits beautiful fish scales. Figure 4(b) is similar to Fig. 4(a) except for the PNR orientation, i.e., a zigzag PNR. In Figs. 4(c) and 4(d), we extract the conductance of armchair and zigzag PNRs in varied magnetic fields at three incident Fermi energies. The oscillation periods are slightly related to the Fermi energies; in Figs. 4(c) and 4(d) we can see that the conductances for different incident energies are not exactly aligned due to the same reason discussed for Fig. 3. We stress in advance that this small variation can hardly suppress the AB-effect-induced giant MR, especially for the first MR peak, as we discuss in the next section. The Fermi energy can also affect the conductance maxima via the density modulation. In addition, at certain Fermi energies, double peaks in the conductance–versus–magnetic-field plot are observed. These double peaks occur when AB destructive interference regions cross resonant peaks with a high density of bound states. The differences between Figs. 4(a) and 4(c) and Figs. 4(b) and 4(d) originate from the anisotropic resonant tunneling behaviors in armchair and zigzag PNRs, shown in Fig. 2.

To clarify the origin of the resonant maxima and different types of minima, we plot the LDOS of armchair PNRs in Figs. 5(a), 5(b), and 5(c), corresponding to points A, B, and C in Fig. 4(a), respectively. It is helpful to distinguish the Fabry-Perot interferences and AB interference effects in the PNRs. We must point out that the LDOSs shown in Fig. 5 are smeared by the Gauss function. In the upper and lower bridges of the armchair PNR ring, Fabry-Perot modes can be formed as a result of the quantum interferences between electron waves moving forward and electron waves moving backward. The presence or absence of these quasibound states is determined by the Fermi energy and ring size L_T. Heuristically, the quantization conditions for bound states are typically given by $n \cdot \lambda = L_T$, where n is an integer and λ is the electron wavelength satisfying the relationship $E_F = h v_F/\lambda$. The density of states develops peaks at $E = n h v_F/L_T$. In Fig. 5(a), the Fermi energy is set to 0.394 eV and the magnetic

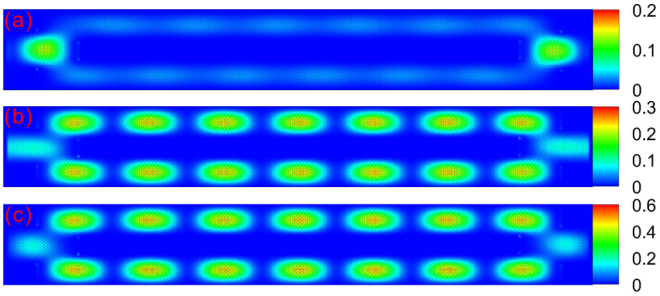

FIG. 5. LDOS of the armchair nanoring. (a), (b), and (c) correspond to points A, B, and C in Fig. 4(a). Here we use a Gauss function to smear the contour plot.

field $B = 0$, which corresponds to the fully blocked case as indicated by point A in Fig. 4(a). The LDOSs are mostly concentrated in the left and right leads, while a few bound states are formed in the two ring bridges. So electrons can hardly propagate through the PNR. We also plot the spatial distribution of LDOSs corresponding to the conduction peak in Fig. 5(b), with $E_F = 0.397$ eV and $B = 0$ [see point B in Fig. 4(a)]. Many more bound states are formed on both sides of the PNR, which can assist electron transmission and, finally, give rise to a conductance peak. Interestingly, with the same E_F level of 0.397 eV, but with the magnetic field increased from 0 to 6.5 T as indicated by point C in Fig 4(a), electron transmission is fully suppressed, while the bound states in the bridges are mainly preserved as shown in Fig. 5(c). This conductance dip is caused by the destructive interferences at the exit interconnection of two paths, i.e., the AB effect. Electrons from upper or lower paths gain different phase shifts arising from the magnetic flux in the PNR. We therefore confirm the AB effect in this PNR.

IV. MAGNETORESISTANCE OF PHOSPHORENE NANORINGS

Next we explore how a finite temperature affects the conductance of PNRs. A thermal broadening function is taken into consideration in the calculation at nonzero temperature. At room temperature (298 K), the oscillation behavior is quite different from that at zero temperature as shown in Fig. 4. The double peaks of conductance at zero temperature disappear and the oscillation amplitudes are reduced. The conductance of the armchair PNR oscillates between $0.2G_0$ and $0.7G_0$ [see Fig. 6(a)]. The oscillation minima of different Fermi energies

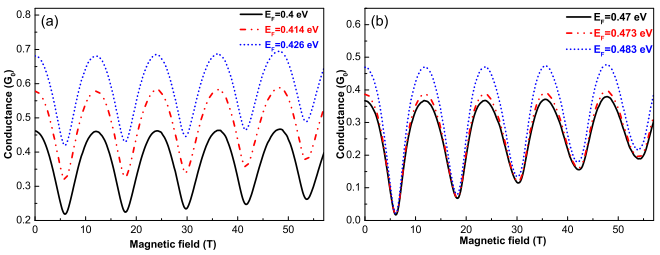

FIG. 6. Relation between the conductance and the magnetic field of (a) armchair and (b) zigzag PNRs with different incident energies at room temperature.

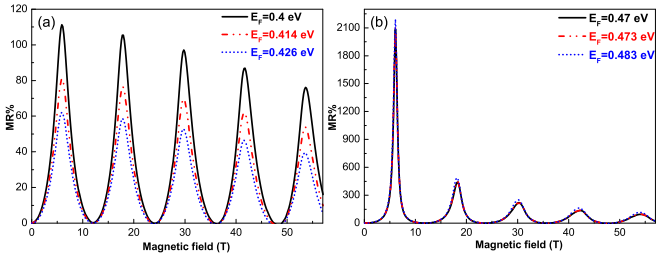

FIG. 7. Magnetic resistance at room temperature of (a) armchair and (b) zigzag PNRs with three incident energies.

almost remain steady in the armchair PNR, while in the zigzag PNR, the minima increase with B [Fig. 6(b)].

Finally, the MR of both armchair and zigzag nanorings are calculated at room temperature (see Fig. 7). It is shown that the conductance of the armchair nanoring exhibits clear AB oscillations [Fig. 7(a)], the period of which also matches well with the expression $\Delta \boldsymbol{B} = 2\pi\phi_0/\bar{S}$. There is a close connection between MR and Fermi energy, i.e., a higher Fermi energy gives rise to a lower MR. The order of the MR for this armchair nanoring is about 100%, which is much smaller than that for an armchair graphene nanoring [43]. While in the zigzag nanoring [see Fig. 7(b)] we find that the MR can be as large as 2000%, which is much greater than that in the armchair nanoring, in agreement with the anisotropy electron property of phosphorene, the MR decays rapidly with the magnetic field, and the MR at different Fermi energies is almost the same.

V. SUMMARY

In this paper, we theoretically demonstrate the AB effect in monolayer PNRs utilizing the TB method and recursive Green's function method. Our numerical results show that the conductance of PNRs oscillates dramatically with the incident Fermi energy and the perpendicular magnetic field. The complex oscillating behavior arises from hybrid effects of the formation of Fabry-Perot modes, formation of Landau levels, and AB interference. The AB oscillation period is dominated by the effect area of the PNR and slightly affected by the incident Fermi energy. When the incident Fermi energy is limited to lower than the bottom of the second subband, the AB effect becomes more pronounced than other effects, leading to a giant MR in the PNR. The MR is highly anisotropic depending on the PNR orientation, i.e., the maximum MR of the zigzag PNR is one order of magnitude larger than that of the counterpart armchair PNR. This investigation sheds new light on the construction of phosphorene-based nanoelectronic devices.

ACKNOWLEDGMENTS

We thank X. Y. Zhou, J. Li, and J. J. Zhu for many useful discussions. We also acknowledge useful suggestions provided by Y. L. Zou. This work was supported by Grants No. 61674145 and No. 11434010 from the NSFC, Grants No. 2015CB921503, No. 2016YFA0202300, and No. 2016YFE0110000 from the MOST of China, and Grant No. QYZDJ-SSW-SYS001 from Chinese Academy of Sciences.

[1] L. Li, Y. Yu, G. J. Ye, Q. Ge, X. Ou, H. Wu, D. Feng, X. H. Chen, and Y. Zhang, Nat. Nanotech. **9**, 372 (2014).

[2] H. Liu, A. T. Neal, Z. Zhu, Z. Luo, X. Xu, D. Tomnek, and P. D. Ye, ACS Nano **8**, 4033 (2014).

[3] S. P. Koenig, R. A. Doganov, H. Schmidt, A. H. Castro Neto, and B. Zyilmaz, Appl. Phys. Lett. **104**, 103106 (2014).

[4] M. Buscema, D. J. Groenendijk, S. I. Blanter, G. A. Steele, H. S. J. van der Zant, and A. Castellanos-Gomez, Nano Lett. **14**, 3347 (2014).

[5] S. Das, W. Zhang, M. Demarteau, A. Hoffmann, M. Dubey, and A. Roelofs, Nano Lett. **14**, 5733 (2014).

[6] W. Lu, H. Nan, J. Hong, Y. Chen, C. Zhu, Z. Liang, X. Ma, Z. Ni, C. Jin, and Z. Zhang, Nano Res. **7**, 853 (2014).

[7] A. S. Rodin, A. Carvalho, and A. H. Castro Neto, Phys. Rev. Lett. **112**, 176801 (2014).

[8] X. Chen, Y. Wu, Z. Wu, Y. Han, S. Xu, L. Wang, W. Ye, T. Han, Y. He, Y. Cai, and N. Wang, Nat. Commun. **6**, 7315 (2015).

[9] V. Tayari, N. Hemsworth, I. Fakih, A. Favron, E. Gaufres, G. Gervais, R. Martel, and T. Szkopek, Nat. Commun. **6**, 7702 (2015).

[10] Y.-L. Zou, J. Song, C. Bai, and K. Chang, Phys. Rev. B **94**, 035431 (2016).

[11] L. Li, F. Yang, G. J. Ye, Z. Zhang, Z. Zhu, W. Lou, X. Zhou, L. Li, K. Watanabe, T. Taniguchi, K. Chang, Y. Wang, X. H. Chen, and Y. Zhang, Nat. Nanotech. **11**, 593 (2016).

[12] A. C. Gomez, L. Vicarelli, E. Prada, J. O. Island, K. L. N. Acharya, S. I. Blanter, D. J. Groenendijk, M. Buscema, G. A. Steele, J. V. Alvarez, H. W. Zandbergen, J. J. Palacios, and H. S. J. van der Zant, 2D Mater. **1**, 025001 (2014).

[13] Q. Wei and X. Peng, Appl. Phys. Lett. **104**, 251915 (2014).

[14] J. O. Island, G. A. Steele, H. S. J. van der Zant, and A. Castellanos-Gomez, 2D Mater. **2**, 011002 (2015).

[15] M. Ezawa, New J. Phys. **16**, 115004 (2014).

[16] R. W. Keyes, Phys. Rev. **92**, 580 (1953).

[17] J. C. Jamieson, Science **139**, 1291 (1963).

[18] V. Tran, R. Soklaski, Y. Liang, and L. Yang, Phys. Rev. B **89**, 235319 (2014).

[19] R. Fei and L. Yang, Nano Lett. **14**, 2884 (2014).

[20] J. D. Wood, S. A. Wells, D. Jariwala, K.-S. Chen, E. Cho, V. K. Sangwan, X. Liu, L. J. Lauhon, T. J. Marks, and M. C. Hersam, Nano Lett. **14**, 6964 (2014).

[21] X. Peng, Q. Wei, and A. Copple, Phys. Rev. B **90**, 085402 (2014).

[22] F. Xia, H. Wang, and Y. Jia, Nat. Commun. **5**, 4458 (2014).

[23] A. N. Rudenko and M. I. Katsnelson, Phys. Rev. B **89**, 201408 (2014).

[24] H. Liu, Y. Du, Y. Deng, and P. D. Ye, Chem. Soc. Rev. **44**, 2732 (2015).

[25] J.-W. Jiang and H. S. Park, Nat. Commun. **5**, 4727 (2014).

[26] M. Engel, M. Steiner, and P. Avouris, Nano Lett. **14**, 6414 (2014).

[27] X. Ling, H. Wang, S. Huang, F. Xia, and M. S. Dresselhaus, Proc. Natl. Acad. Sci. USA **112**, 4523 (2015).

[28] S. B. Lu, L. L. Miao, Z. N. Guo, X. Qi, C. J. Zhao, H. Zhang, S. C. Wen, D. Y. Tang, and D. Y. Fan, Opt. Express **23**, 11183 (2015).

[29] R. Zhang, X. Y. Zhou, D. Zhang, W. K. Lou, F. Zhai, and K. Chang, 2D Mater. **2**, 045012 (2015).

[30] X. Y. Zhou, W.-K. Lou, F. Zhai, and K. Chang, Phys. Rev. B **92**, 165405 (2015).

[31] X. Y. Zhou, R. Zhang, J. P. Sun, Y. L. Zou, D. Zhang, W. K. Lou, F. Cheng, G. H. Zhou, F. Zhai, and K. Chang, Sci. Rep. **5**, 12295 (2015).

[32] J. Qiao, X. Kong, Z.-X. Hu, F. Yang, and W. Ji, Nat. Commun. **5**, 4475 (2014).

[33] N. Gillgren, D. Wickramaratne, Y. Shi, T. Espiritu, J. Yang, J. Hu, J. Wei, X. Liu, Z. Mao, K. Watanabe, T. Taniguchi, M. Bockrath, Y. Barlas, R. K. Lake, and C. N. Lau, 2D Mater. **2**, 011001 (2015).

[34] X. Wang, A. M. Jones, K. L. Seyler, V. Tran, Y. Jia, H. Zhao, H. Wang, L. Yang, X. Xu, and F. Xia, Nat. Nanotech. **10**, 517 (2015).

[35] Y. Deng, Z. Luo, N. J. Conrad, H. Liu, Y. Gong, S. Najmaei, P. M. Ajayan, J. Lou, X. Xu, and P. D. Ye, ACS Nano **8**, 8292 (2014).

[36] M. Buscema, D. J. Groenendijk, G. A. Steele, H. S. J. van der Zant, and A. Castellanos-Gomez, Nat. Commun. **5**, 4651 (2014).

[37] J. Dai and X. C. Zeng, J. Phys. Chem. Lett. **5**, 1289 (2014).

[38] N. Hemsworth, V. Tayari, F. Telesio, S. Xiang, S. Roddaro, M. Caporali, A. Ienco, M. Serrano-Ruiz, M. Peruzzini, G. Gervais, T. Szkopek, and S. Heun, Phys. Rev. B **94**, 245404 (2016).

[39] P. Masih Das, G. Danda, A. Cupo, W. M. Parkin, L. Liang, N. Kharche, X. Ling, S. Huang, M. S. Dresselhaus, V. Meunier, and M. Drndi, ACS Nano **10**, 5687 (2016).

[40] Y. Aharonov and D. Bohm, Phys. Rev. **115**, 485 (1959).

[41] A. Mreńca-Kolasińska, S. Heun, and B. Szafran, Phys. Rev. B **93**, 125411 (2016).

[42] W. Tian and S. Datta, Phys. Rev. B **49**, 5097 (1994).

[43] V. H. Nguyen, Y. M. Niquet, and P. Dollfus, Phys. Rev. B **88**, 035408 (2013).

[44] D. Faria, R. Carrillo-Bastos, N. Sandler, and A. Latg, J. Phys.: Condens. Matter **27**, 175301 (2015).

[45] I. Romanovsky, C. Yannouleas, and U. Landman, Phys. Rev. B **85**, 165434 (2012).

[46] C. Yannouleas, I. Romanovsky, and U. Landman, J. Phys. Chem. C **119**, 11131 (2015).

[47] Y. Imry and R. Landauer, Rev. Mod. Phys. **71**, S306 (1999).

[48] S. Datta, *Electronic Transport in Mesoscopic Systems* (Cambridge University Press, Cambridge, UK, 1995).